ARCHIVES OF ACOUSTICS Vol. 49, No. 1, pp. 95–106 (2024), doi: 10.24425/aoa.2024.148767

Research Paper

The Influential Factors and Prediction of Kuroshio Extension Front on Acoustic Propagation-Tracked

Weishuai XU[(1)], Lei ZHANG[(2)*], Hua WANG[(2)]

[(1)] *No. 5 Student Team, Dalian Naval Academy*
Dalian, Liaoning, China; e-mail: xuweishuai2022@163.com

[(2)] *Department of Military Oceanography and Hydrography and Cartography*
Dalian Naval Academy
Dalian, Liaoning, China

*Corresponding Author e-mail: stone333@tom.com

(*received May 16, 2023; accepted September 14, 2023; published online December 19, 2023*)

The Kuroshio Extension front (KEF) considerably influences the underwater acoustic environment; however, a knowledge gap persists regarding the acoustic predictions under the ocean front environment. This study utilized the high-resolution ocean reanalysis data (JCOPE2M, 1993–2022) to assess the impact of the KEF on the underwater acoustic environment. Oceanographic factors were extracted from the database using the Douglas-Peucker algorithm, and acoustic propagation characteristics were obtained using the Bellhop ray-tracing model. This study employed a backpropagation neural network to predict the acoustic propagation affected by the KEF. The depth of the acoustic channel axis and the vertical gradient of the transition layer of sound speed were identified as the fundamental factors influencing the first area of convergence, with correlations between the former and the distance of the first convergence zone ranging from 0.52 to 0.82, and that for the latter ranging from −0.42 to −0.7. The proposed method demonstrated efficacy in forecasting first convergence zone distances, predicting distances with less than 3 km error in >90% of cases and less than 1 km error in 68.61% of cases. Thus, this study provides a valuable predictive tool for studying underwater acoustic propagation in ocean front environments and informs further research.

Keywords: Kuroshio Extension front; acoustic propagation; convergence zone prediction.

1. Introduction

The Kuroshio Current, a warm ocean current, flows eastward off the coast of Japan at around 35°N and 141°E and expands eastwards at ~165°E. The eastern segment of this current, termed the Kuroshio Extension (YASUDA, 2003), is characterized by a zonal jet with substantial amplitude bending, and its location is presented in Fig. 1. The warm and highly saline Kuroshio Current flowing from the south merges with the cold and slightly saline Oyashio Current coming from the north in the eastern region of Japan. The convergence of these two western boundary currents forms a distinct transition zone between subtropical and subpolar gyres, designated as the Kuroshio Extension

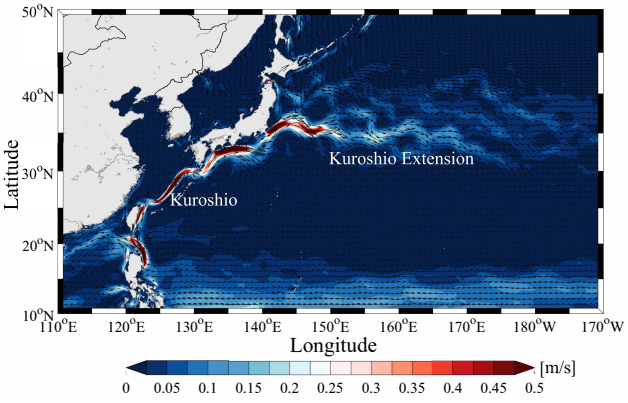

Fig. 1. Schematic diagram of the Kuroshio and Kuroshio Extension (base map: multiyear averaged flow field).

front (KEF) (Chen, 2008). As an exceptionally prominent mesoscale phenomena across global oceans, the KEF demonstrates unique physical and chemical attributes that greatly impact underwater acoustic propagation. By examining the acoustic propagation at the KEF, we can gain a deeper understanding of the influence of the marine environment on sound transmission. This study provides essential guidance for applications such as underwater acoustic communication and sonar detection. Furthermore, predicting acoustic propagation variables in the oceanic front environment contributes to technical assistance for ocean environmental monitoring and the development of marine sonar detection technology.

The spatial distribution of the sound speed field experiences rapid alterations in an ocean front with a narrow transition zone of seawater types characterized as an ocean front discontinuity (Cheney, Winfrey, 1976). Such a phenomenon considerably affects underwater acoustic propagation and associated transmission losses. As Etter (2013) initially posited, the impact of ocean fronts on acoustic propagation is exemplified through the surface sound speed and the structure of the acoustic channel axis. Prior research has comprehensively scrutinized the impacts of ocean fronts on acoustic propagation (Dreini, Jensen, 1990; Mellberg *et al.*, 1991; Rousseau *et al.*, 1982; Shapiro *et al.*, 2014), revealing that the morphology and position of ocean fronts have a significant impact on sound propagation, which results in an increase in transmission loss of 6–20 dB. Ozanich *et al.* (2022) investigated the underwater acoustic propagation of low-frequency sound waves with low grazing angles via the New England Shelf Front in spring, demonstrating the sensitivity of low-frequency propagation to the geometric configurations of ocean fronts. Being one of the major ocean fronts in the northwest Pacific, the acoustic characteristics of the KEF have also received considerable attention. Liu *et al.* (2015) utilized the absolute gradient method to examine the spatial information of the KEF front axis from WOA13 data and explored the acoustic propagation characteristics within the front area, identifying a strong influence of the sound source depth on the underwater axis of the acoustic channel. Additionally, Chen *et al.* (2017) developed a sound speed characteristic model using ARGO and WOA data, which demonstrated that the KEF modifies acoustic propagation by varying the depth of the acoustic channel axis. A collaborative experiment by Liu *et al.* (2021) in marine acoustics and physical oceanography in the northwest Pacific Ocean revealed a sharp rise in acoustic transmission loss toward the side of the cold-water mass when the sound source was positioned within the front area.

Artificial neural networks (ANNs) represent a fundamental machine learning model, with the advancement of machine learning; these neural network models have been progressively refined in recent years. The adaptability of ANNs has increasingly improved. Their ability to adapt to a variety of complex underwater environments and signal conditions has resulted in the extensive implementation of ANNs; additionally, ANNs have achieved widespread applications in the field of underwater acoustics domain. Doan *et al.* (2020) employed convolutional neural networks for target recognition and classification within a passive sonar dataset, ensuring the overall accuracy of 98.85% at 0 dB signal-to-noise ratio. Lee-Leon *et al.* (2021) designed a receiver system based on a deep belief network and, through simulation modeling and sea trials, demonstrated that the receiver system exhibited superior performance in channels affected by the Doppler effect and multipath propagation. Lee *et al.* (2022) introduced a supervised learning-based method for quantifying uncertainty in transmission loss and assessed its ability to simulate long-distance underwater propagation using different computational models, environmental scenarios, and sources and levels of uncertainties.

As the understanding of the KEF advances, along with the ascent of neural networks, the prediction of underwater acoustic propagation based on KEF oceanographic variables is emerging as an area of research deserving attention. However, the current dearth of studies on the impact of the KEF on the underwater acoustic environment and the considerable gaps in the neural network-based prediction of acoustic propagation in ocean front environments necessitate further investigation. Therefore, this study employs high-resolution ocean reanalysis data to analyze the vertical characteristics of the KEF and identify the frontal zone with the most potent KEF using statistical analysis methods. The factors affecting acoustic propagation in proximity to multiple factors near the frontal zone are investigated in Sec. 3. The study examines the primary oceanic structures influencing acoustic propagation in the KEF region. Based on backpropagation (BP) neural networks, a convergence zone prediction model is constructed for the KEF environment in Sec. 4, with the aim of providing benchmarks for future acoustic propagation forecasts in marine front environments.

2. Materials and methods

2.1. Materials

2.1.1. Reanalysis data

The temperature and salinity data used in this study were derived from the high-resolution and high-analysis product JCOPE2M (Japan Coastal Ocean Predictability Experiment 2 Modified) based on the Princeton Ocean Model and was provided by the Japan

Agency for Marine-Earth Science and Technology (Miyazawa *et al.*, 2017; 2019). The regional coverage includes the northwest Pacific Ocean. The dataset used in this research spans from January 1, 1993, to August 31, 2022, with a horizontal resolution of 1/12° and 46 σ-levels in the vertical dimension. This dataset has high resolution and high accuracy and has been widely applied in the study of mesoscale phenomena and flow fields in the Kuroshio region (Chang *et al.*, 2015; 2018; Liu *et al.*, 2019).

2.1.2. Multiyear average flow field data

The Navy Coupled Ocean Data Assimilation system, integrating the hybrid coordinate ocean model and multiple observational datasets, was harnessed by the United States Naval Research Laboratory to generate a 22-year average flow field from 1994 to 2015. This dataset was used to display the position of the Kuroshio Extension. The spatial resolution of this system is 1/12° horizontally and consists of 40 nonuniformly and vertically spaced layers (Chassignet *et al.*, 2007). Based on the hybrid isopycnal-sigma-pressure (generalized) coordinate ocean assimilation model, the average flow field serves as a valuable reference for reporting the velocity and location of Kuroshio.

2.1.3. Bathymetric data

The bathymetric data used for underwater acoustic propagation simulation in this study were obtained from the joint release of the ETOPO1 bathymetric model, bearing a grid size of $1' \times 1'$. This model integrates global land topography and ocean depth data based on various relevant models and measured data (Amante, Eakins, 2009). The majority of the ocean depth data in this model are derived from the bathymetric model released by the Scripps Institution of Oceanography, while the land topography data mainly come from the GTOPO30 global digital elevation model with a resolution of 30 arc-s. The study area based on ETOPO1, as illustrated in Fig. 2, covers the region from 142° to 162°E and 33° to 37°N.

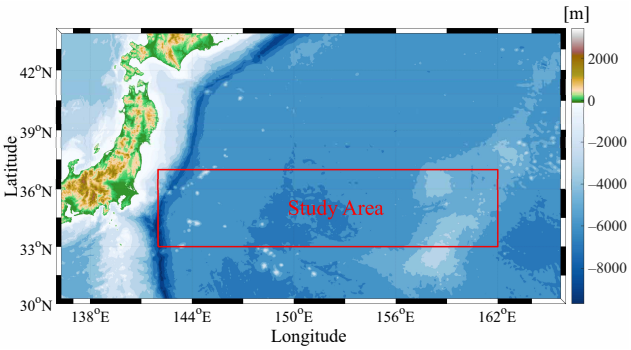

Fig. 2. Topography of the study area.

2.2. Methods

This study uses reanalyzed temperature and salinity data to explore the KEF environment. The Mackenzie empirical formula, which was introduced in 1981, was utilized to calculate the sound speed field in the KEF environment. Additionally, the absolute gradient method was employed to extract the temperature and salinity frontal information near the KE region. The variation of the KEF strength with depth is examined, and a cross-section with the highest horizontal temperature gradient (HTG) in the KEF area is selected as the focus of the study from the daily JCOPE2M dataset. Based on Etter's (2013) work on the impact of ocean fronts on acoustic propagation and fundamental propagation modes for both near and distant acoustic propagation, calculations were performed for five environmental and two acoustic propagation parameters (Table 1). A correlation heatmap was created to statistically analyze the significant impact of the environmental parameters on underwater acoustic propagation. Based on these findings, an acoustic propagation prediction model for the KEF environment was constructed using a BP neural network.

2.2.1. Calculation methods for environmental parameters

The KEF is formed by the interaction between the warm and salty Kuroshio Extension and the cold and fresh coastal currents. Therefore, this study uses the

Table 1. Factors considered in this study and their calculation methods.

	Parameters	Calculation method
Environmental parameters	Horizontal temperature gradient	Absolute gradient method
	Horizontal salinity gradient (HSG)	
	Acoustic channel axis depth (ACAD)	Douglas–Peucker (DP) algorithm
	Sonic layer depth (SLD)	
	Transition layer of sound speed (TLSS)	
Underwater acoustic propagation parameters	Short-range detection (SRD) distance	Propagation distance of underwater acoustic at the figure of merit factor level of 90 dB
	First convergence zone distance	Horizontal distance to the first minimum value of underwater acoustic transmission loss

absolute gradient method to determine the horizontal temperature and salinity gradients and the absolute gradient as a measure of the KEF strength. This method is widely used in oceanic frontal research (Dong *et al.*, 2006; Liu *et al.*, 2015; Wang *et al.*, 2020; Yu *et al.*, 2020). The equation is stated as:

$$\text{Grad} = \sqrt{(\partial\phi_U/\partial x)^2 + (\partial\phi_V/\partial y)^2}, \tag{1}$$

where $\partial\phi_U$ represents the meridional difference of the study variable (temperature and salinity), $\partial\phi_V$ represents the zonal difference of the study variable, ∂x represents the meridional distance, and ∂y represents the zonal distance.

Furthermore, this study employs the Douglas–Peucker algorithm to simplify the underwater acoustic field environment into a three-layer sound velocity structure, as proposed by Urick (1975). This includes extraction of the sonic layer depth and the transition layer of sound velocity. The transition layer of sound velocity refers to the vertical gradient within the sound speed interface. The Douglas–Peucker algorithm is a classic line simplification algorithm that can extract characteristic points in the sound velocity structure based on a fixed distance threshold. It uses the vertical distance as a simplification indicator, which ensures the shape characteristics of the sound velocity profile. Moreover, when the distance threshold is set, the extraction of characteristic points remains relatively consistent.

2.2.2. Calculation methods for acoustic propagation factors

This study considers both long-range and short-range sonar detection methods. The horizontal distance from the first convergence zone (FCZ) and the horizontal distance of a passive sonar's figure of merit (FOM) factor, which is 90 dB, are extracted as the acoustic propagation factors. The convergence zone is a major acoustic propagation mode for long-range sonar detection, and the horizontal detection distance at a 90 dB FOM factor denotes the detection distance for short-range detection. Both factors are computed using the Bellhop ray-tracing model (Porter, 2011), which is based on geometric and physical propagation laws and can accommodate various types of rays, including Gaussian beams. The parameters for the Bellhop model used herein were set according to Table 2, where the seafloor parameters were derived from the acoustic properties of sediment provided by Hamilton (1980).

Table 2. Parameter settings for the Bellhop ray-tracing model.

Sound source parameters	Source frequency		Grazing angle range
	1 kHz		–45°–45°
Seafloor parameters	Density	Compressional wave velocity	Attenuation coefficient
	1.421 g/cm^3	1520 m/s	0.12

2.2.3. Factor analysis and prediction methods

After determining the aforementioned seven factors (Table 1), we constructed a correlation heatmap for statistical analysis, representing the relations between variables. Different colors were used to encode the Pearson correlation coefficients between each pair of variables. This study aims to investigate the impact of five oceanographic environmental factors on acoustic propagation in the ocean frontal zone. Correlation analysis results help in selecting the highly correlated factors of acoustic propagation to construct a prediction model using the BP neural network. The model proposed herein is a typical supervised learning algorithm that employs the learning process of the error BP algorithm to autonomously learn the complex relation between the sound waves and environmental factors, thereby improving the accuracy and precision of the predictions. Moreover, the model provides valuable insights for the comprehensive analysis of acoustic propagation forecasts.

3. Results of the statistical analysis between KEF and acoustic propagation

3.1. Variation characteristics of KEF strength with depth

The HTG in the KE region serves as a principal method for measuring KEF. Extensive research has been conducted on the variation characteristics of the KE temperature front (Seo *et al.*, 2014; Wang *et al.*, 2016; 2020; Yu *et al.*, 2020). However, there is limited understanding of the evolving trends of subsurface KEF characteristics beneath the sea surface. In this study, we combine the KEF range offered by Kida *et al.* (2015) and adopt the method proposed by Sugimoto *et al.* (2014). We utilize two indicators, namely, average HTG and maximum HTG, within the region of 142°–162°E and 33°–37°N as the measures of the KEF strength. For a comprehensive representation of the KEF strength, we statistically analyze the depths at which these two indicators reach their maximum values, and their frequency and distribution are plotted in Fig. 3.

The findings indicate that the KEF strength increased and the strength exhibited an increasing trend followed by a decreasing trend with depth. The peak intensity of KEF frequently occurred at depths of 300 and 400 m, with strengths of 0.8395 and 0.7656°C/km, respectively. Below 800 m, the frequency approached 0, indicating that the peak KEF strength occurred most frequently at depths of 300 and 400 m.

This finding aligns with the conclusion of Liu *et al.* (2015), which demonstrates that the intensity of KEF

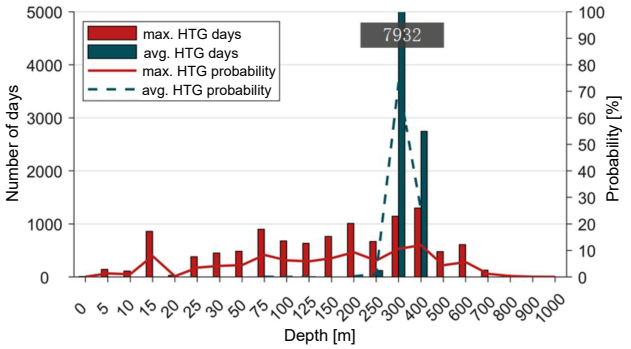

Fig. 3. Statistics and frequency distribution of the strongest depth frequency in KEF.

is considerably higher between 200 and 500 m compared to other water layers. Similarly, the average temperature gradient showcases a pronounced high-value zone at 300 m, indicating the largest range of the KEF at this depth. The maximum average temperature gradient in this area is 0.0646°C/km.

Thus, this study demonstrates that the utilization of the HTG at a depth of 300 m provides improved accuracy in determining the precise location of the KEF. This methodology is more effective compared to solely relying on surface intensity and position as it uncovers a comprehensive understanding of the variation characteristics exhibited by the KEF.

This study categorized the intensity levels of the KEF based on a maximum HTG of 300 m. Combining statistical data from JCOPE daily data, the KEF with a maximum HTG between 0 and 0.2°C/km were defined as weak fronts, accounting for 22.0% of the total recorded days. Further, the KEF with a maximum HTG between 0.2 and 0.3°C/km were classified as moderate intensity fronts (50.7%), whereas those with a gradient between 0.3 and 0.9°C/km were classified as strong fronts (27.3%). Three different months were selected to examine acoustic propagation under varying frontal conditions (Table 3), and a correlation heatmap was plotted to illustrate the impact of ocean fronts on the oceanic structure and acoustic propagation.

Table 3. Representative month for three intensity temperature gradients.

Intensity	Month	Temperature gradient [°C/km]	Monthly average [°C/km]
Strong	2012.07	0.304(7.14)–0.831(7.30)	0.5498
Middle	2002.12	0.220(12.1)–0.315(12.5)	0.2793
Weak	2022.08	0.130(8.16)–0.388(8.10)	0.1874

3.2. Statistical analysis of the impact of environmental parameters on underwater acoustic propagation in the KEF environment

To pinpoint the location of the most potent KEF, the grid where it transpires is identified using daily data, and a section spanning 12 nodes (~1°) from both the warm and cold sides of KEF is selected as the research scope for the given day. Subsequently, sound sources are arranged in the first 11 nodes, and information regarding ocean structure alterations and acoustic propagation distance between the outliers is documented (Fig. 4). Throughout the research process, only the alterations in the sound field environment of adjacent grids are considered. For instance, when the sound source is located at Station A1, the sound field environment is constructed using the sound speed profile between the A1 and A2 grids. Thereafter, 10 sets of sound speed profiles from A2 are replicated along the acoustic propagation direction to construct the environmental sound field file. This methodology aids in circumventing any interference caused by the changes in the ocean structure at other locations on acoustic propagation. Considering the practical scenarios in which sonar is employed, this study sets the deployment depth of the sound source at 30 m and the receiver depth at 150 m.

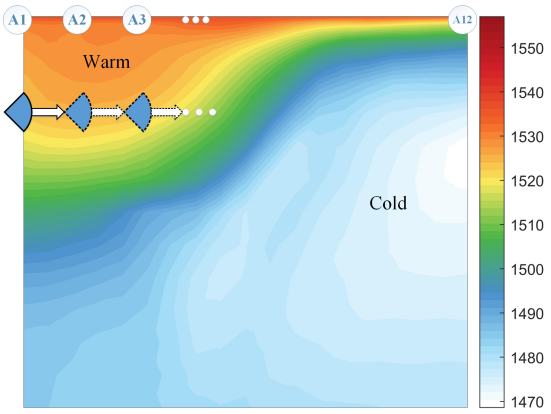

Fig. 4. Schematic of the research methodology (the base figure represents the sound velocity distribution of 2012.7.30 section [m/s]).

Subsequences of 5 environmental parameters and 2 underwater acoustic propagation parameters, with each subsequence containing 11 datasets, were constructed. The daily subsequences of the mentioned parameters are concatenated into monthly sequences for correlation analysis using the equations:

$$X = x_1 \oplus x_2 \oplus \ldots \oplus x_N, \tag{2}$$

$$r = \frac{\sum_{i=1}^{M}(X_i - \overline{X})(Y_i - \overline{Y})}{\sqrt{\sum_{i=1}^{M}(X_i - \overline{X})^2}\sqrt{\sum_{i=1}^{M}(Y_i - \overline{Y})^2}} \quad (M = 11N), \tag{3}$$

where x and y symbolize two factors, n signifies the number of days in the current month, and the $\oplus$ operator indicates the sequence concatenation. The correlation analysis results are displayed in Fig. 5, where

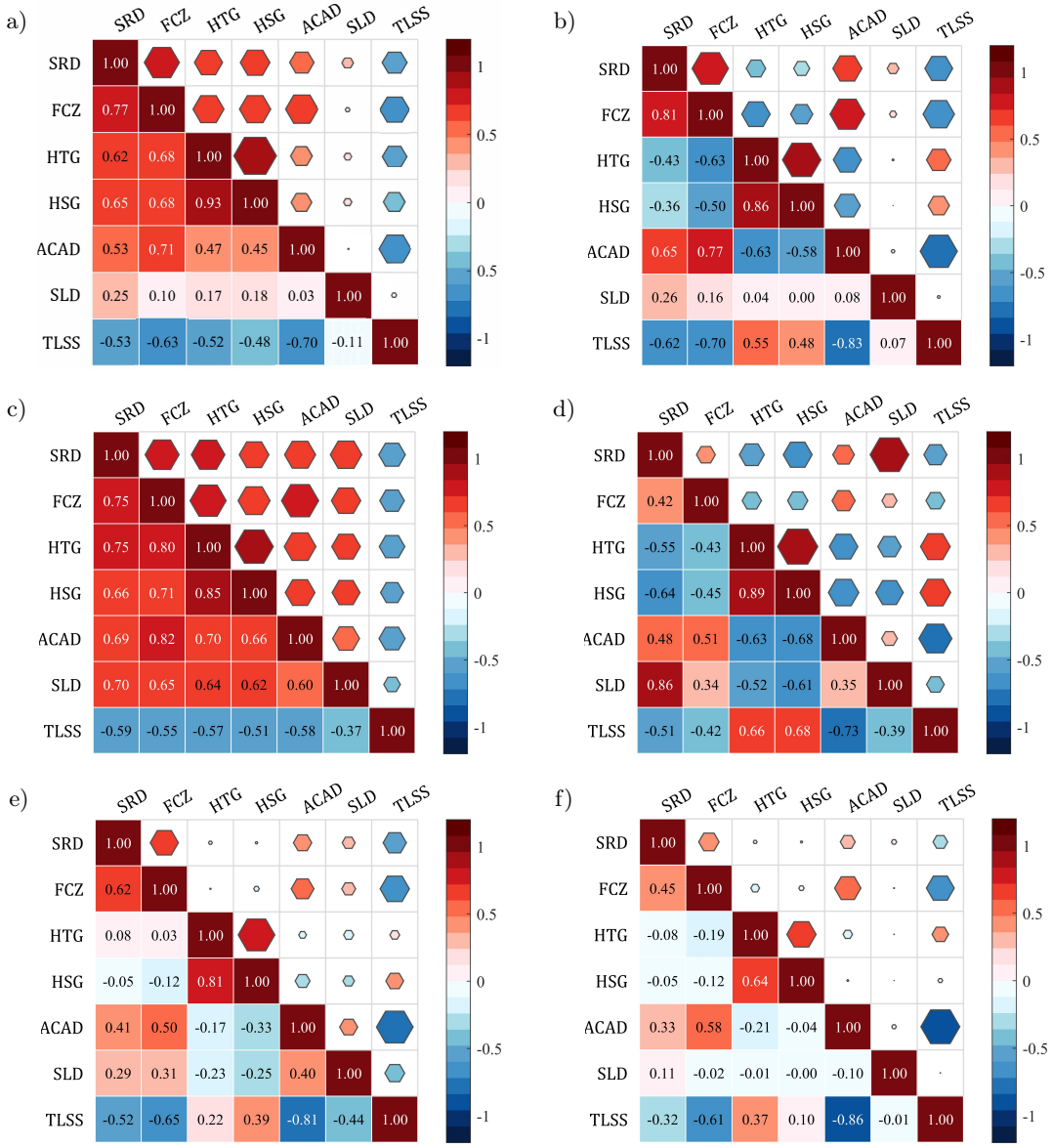

Fig. 5. Heatmap of correlation between sea structure and the underwater acoustic propagation parameters of Kuroshio Extension front presented at three different intensities. Panels (a) and (b) display data from July 2012 with warm-water side to cold-water side and cold-water side to warm-water side orientations, respectively. Panels (c) and (d) present data from December 2002, with warm-water side to cold-water side and cold-water side to warm-water side orientations, respectively. Panels (e) and (f) display data from August 2022, with warm-water side to cold-water side and cold-water side to warm-water side orientations, respectively.

the correlation heatmap translates the values in the correlation matrix into colors based on specific rules, thus visualizing the correlation through color variations. Warm colors suggest a positive correlation, and cold colors denote a negative correlation. The color and data of each cell in the heatmap represent the correlation between the row and column variables. The primary conclusions are:

(1) When the sound source emits sound waves from the warm-water side toward the cold-water side, the horizontal temperature and salinity gradients considerably influence the detection range at the strong KEF (July 2012) and the moderate KEF (December 2002). The correlation coefficients for the temperature gradient are 0.62 and 0.75, whereas for the salinity gradient, they are 0.65 and 0.66, respectively. Thereafter, we focused on the depth of the acoustic channel axis, exhibiting a positive correlation of 0.53 and 0.69. The vertical gradient of the transition layer of sound speed demonstrates a negative correlation with absolute correlation coefficients exceeding 0.5. The impact of the sound layer depth on underwater acoustic propagation displays noticeable seasonal characteristics. For the moderate KEF in winter, the surface sound layer

is thicker, resulting in a high correlation coefficient of 0.7 between the sound layer depth and the short-range detection distance in December. Conversely, in July, a weak correlation is seen. At the weak KEF (August 2022), the correlation between the horizontal temperature-salinity gradient and the short-range detection distance considerably decreases and becomes unrelated. The factors with higher correlation denote the vertical gradient of the transition layer of sound speed and the depth of the acoustic channel axis, exhibiting a negative correlation of −0.53 and a positive correlation of 0.41, respectively.

(2) When the sound source emits sound waves from the warm-water side toward the cold-water side, the depth of the acoustic channel axis correlates most strongly with the FCZ distance, with a maximum positive correlation coefficient of 0.82. Thereafter, the vertical gradient of the transition layer of sound speed, which displays a significant negative correlation, has a maximum value of −0.63. The horizontal temperature-salinity gradient highly correlates with the convergence zone than within the range of the source reception depth, indicating that as the sound source migrates from the KEF to the cold-water side with the reduced KEF strength, the horizontal distance between the FCZ distance and the sound source becomes shorter.

(3) When the sound source emits sound waves from the cold-water side toward the warm-water side, the vertical gradient of the transition layer of sound speed greatly impacts underwater acoustic propagation at short range, with negative correlation coefficients of −0.62, −0.51, and −0.32. The correlation coefficient decreases with the KEF strength. The depth of the acoustic channel axis displays the highest positive correlation of 0.65 with the short-range underwater acoustic propagation distance. The horizontal temperature-salinity gradient exhibits a negative correlation with the short-range underwater acoustic propagation distance when the sound source is located on the warm-water side, with correlation coefficients ranging from −0.3 to −0.6. The sound layer depth exhibits the strongest correlation in December 2002, reaching 0.86, while the remaining periods display weak or no correlation.

(4) The statistical results are analogous when the sound source is on the warm-water side. The vertical gradient of the transition layer of sound speed and the depth of the acoustic channel axis pose the most significant impact on the convergence zone, with absolute correlation coefficients ranging from 0.4 to 0.8. Subsequently, the horizontal temperature-salinity gradient, which shows different degrees of negative correlation, ranged between −0.4 and −0.6 at strong and moderate KEF intensities. The correlation of the temperature gradient is slightly higher (by 0.13) than that of the salinity gradient by suggesting that as the sound source migrates from the KEF to the warm-water side with a decrease in the KEF strength, the horizontal distance between the FCZ and the sound source lengthens.

Based on the above analysis, we concluded that the KEF has a more pronounced effect when the sound source is situated on the warm-water side. Moreover, the correlation between the HTG and HSG on the warm-water side and the underwater acoustic propagation parameters is 0–0.3 higher than on the cold-water side. Among the factors examined, the depth of acoustic channel axis and the vertical gradient of the transition layer of sound speed have the most significant influence on the convergence zone distance. The correlation between the former and the distance of the FCZ can reach 0.52–0.82, whereas the latter ranges from −0.42 to −0.7. Moreover, the FCZ distance has a slightly higher correlation of HTG (0–0.13) compared to HSG. Nevertheless, under weak front conditions, the temperature-salt gradient is either weakly correlated or uncorrelated with underwater acoustic propagation. Additionally, the sound layer exhibits noticeable seasonal variation characteristics, posing a substantial impact on the short-range detection distance (up to 0.86) in winter and a weak correlation in July and August.

4. Establishment and validation of the underwater acoustic propagation prediction model

Construction of the underwater acoustic propagation prediction model based on the BP neural network follows the same acoustic field construction method as described in Sec. 3. Over a 30-year period, the JCOPE2M dataset from February and August were utilized to construct the input sequences, encompassing four datasets with the sound source positioned on the warm-water and cold-water sides. Based on the statistical analysis of the correlations between the input parameters, the five environmental parameters were analyzed as input features for the month of February, while for the month of August, four environmental parameters, excluding the sound layer depth, were considered as the input features. The output features of the model include the distance to the FCZ distance and the short-range detection distance.

After performing normality tests on the data and eliminating outliers based on the 3σ rule, the selected sequences were randomly sorted and split into training and testing sets at a ratio of 9:1. The BP neural network was employed to estimate initial predictions on the first convergence distance of the ocean front zone. This is a standard algorithm used to train ANNs. By training with sample data and constant adjustments of network weights and thresholds, the error function can be minimized in the direction of a negative gradient, thereby approaching the desired output. In this

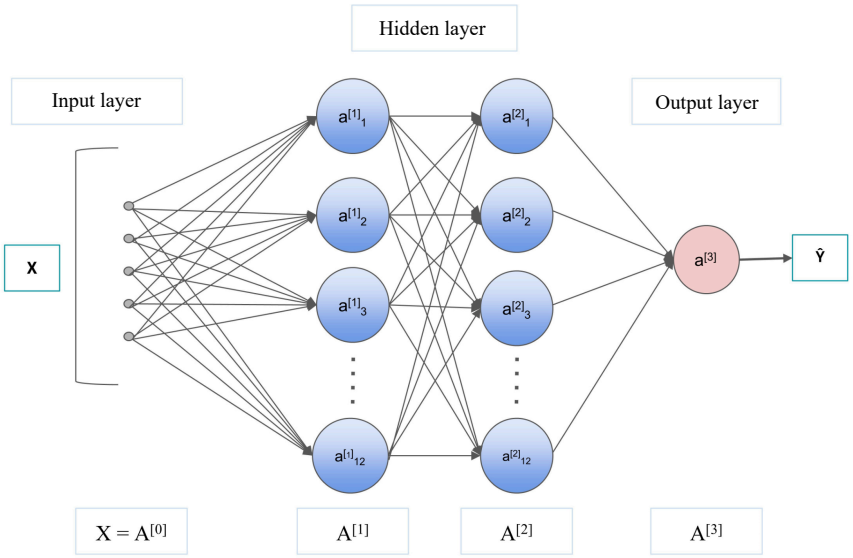

Fig. 6. Structural diagram of the backpropagation (BP) neural network.

study, the sigmoid function was utilized for the hidden and output layers. Two hidden layers were set, and a training algorithm was used for optimization iteration. The following empirical equation was used to determine the number of nodes in the hidden layer:

$$m = \sqrt{n + l} + \partial, \tag{4}$$

where m signifies the number of nodes in the hidden layer, n represents the number of nodes in the input layer, l represents the number of nodes in the output layer, and ∂ is a constant ranging from 1 to 10, which determines the range of hidden layer nodes. Multiple network structures are created within this range, and each network with varying nodes in the hidden layer is modeled and trained. The mean square error is computed for each network, and the optimal number of nodes in the hidden layer is determined to be 12 based on the lowest mean square error. The structure of the constructed neural network is illustrated in Fig. 6.

When the sound source is positioned on the warm side, a scatter plot is drawn between five parameters and the distance to the FCZ (Fig. 7). The correlation between the depth of the acoustic channel axis and the distance to the FCZ distance displayed the best continuity, suggesting that a deeper acoustic channel axis generally produces a convergence zone at a more distant location. The distribution of the sound layer depth is similar to the former but more spread out. The horizontal thermohaline gradient shows a trend of increasing and then decreasing with the distance to the convergence zone, with the maximum value appearing at ~60 km. The vertical gradient of the transition layer of sound speed exhibits a decreasing trend with the convergence zone, which is in accordance with the conclusions derived in the previous section.

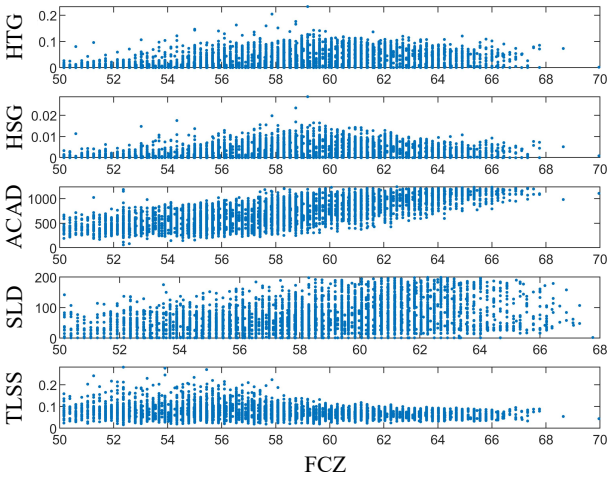

Fig. 7. Scatter plot between the convergence zone and the fitting factors.

Using the constructed BP neural network, we modeled and predicted the convergence zone distance in the KEF environment in February. The regression and fitting results of the prediction are presented in Fig. 8. We observed that the predicted outcomes were primarily clustered near the regression line, and the trend variation between the predicted values and the input values was generally consistent. The regression coefficient (R) was 0.84, indicating a good prediction effect.

The training outcomes of the remaining three datasets are similar to the first one. Table 4 presents the fitting performance of the four datasets evaluated in terms of the mean absolute error (MAE) and the coefficient of determination (R^2), both of which reflect the degree of agreement between the predicted and actual datasets; smaller values imply superior fit-

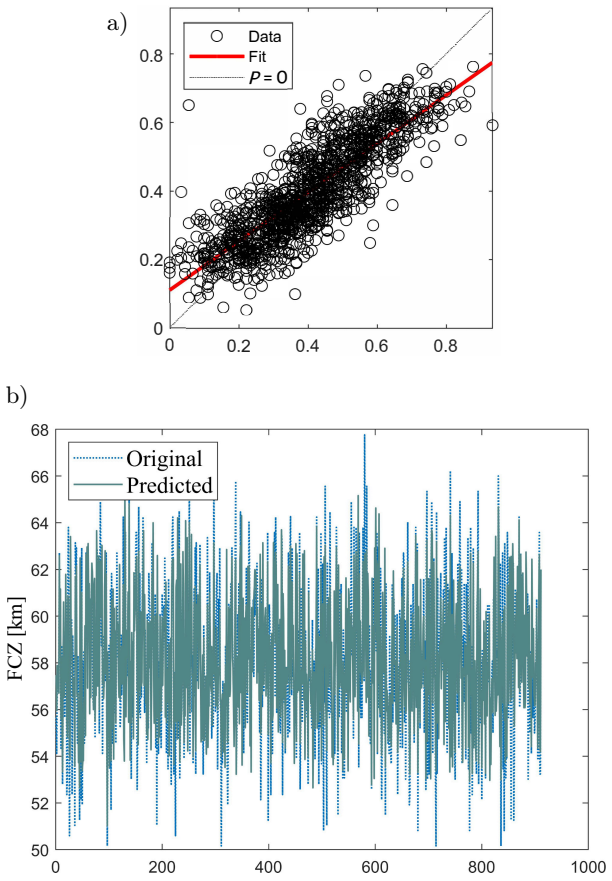

Fig. 8. Prediction effect of BP neural network: a) prediction regression scatter plot (abscissa denotes the normalized original distance and ordinate charts the normalized predicted distance); b) line graph comparing the predicted distance and the original distance of the FCZ distance (the horizontal coordinate is the number of data).

ting performance. The percentage deviation between the predicted and original datasets is also provided. Overall, the results observed that the predictive performance of the August dataset is superior, with an MAE of ~0.3–0.4 km lower than that of the February dataset. When the sound source is situated on the cold-water side, the frequency of test data with prediction errors under 1 km reaches 68.61% and that with errors under 2 km surpasses 90%, which is higher than that of the February dataset on the same cold-water side (49.24 and 76.52%, respectively). As there is a certain thickness of the sound layer in February, the distribution of convergence distance is more dispersed, resulting in an R^2 of >0.7 for the warm-water side of February, offering the best fitting effect among the four datasets. However, the proportion of test data with training errors of less than 1 km is less than half.

Similarly, we follow the same forecasting process for modelling and predicting underwater acoustic propagation distances at short range (Table 5). The occurrence of the sound layer is closely associated with the season, and the prediction accuracy of the short-range detection distance exhibits significant seasonal variations. In the summer months, the surface layer in the KE region is dominated by sound ducts, where sound rays rapidly bend downward, resulting in relatively shorter horizontal detection distances. Therefore, when the sound source is located on the warm-water and cold-water sides in August, the probability of the prediction error being less than 3 km is extremely high, exceeding 99%. On the contrary, during the winter season, the surface layer is typically dominated by the sound layer. Based on the BP neural network, the probability of the prediction error at less than 3 km was ~80%.

In conclusion, this research assembled four datasets with sound sources located on the cold-water and warm-water sides of the KEF for the months of February and August over a span of 30 years. The BP neural network was employed to establish a prediction model for the FCZ distance and the short-range detection distance. The results verified that the convergence zone distance and the short-range detection distance

Table 4. Predictive performance of the four datasets.

Month	Sound position	Train		Test		Predicted error [%]		
		MAE	R^2	MAE	R^2	<1 km	<2 km	<3 km
2	W	1.35	0.71	1.39	0.71	45.77	75.30	90.67
	C	1.26	0.61	1.25	0.58	49.24	76.52	90.65
8	W	0.99	0.70	0.98	0.65	59.73	87.77	96.13
	C	0.50	0.37	0.51	0.37	68.61	91.62	97.85

Table 5. Prediction performance of the source reception depth distance based on the backpropagation neural network.

Month	Sound position	Train		Test		Predicted error [%]		
		MAE	R^2	MAE	R^2	<1 km	<2 km	<3 km
2	W	1.71	0.47	1.80	0.43	39.45	68.72	83.36
	C	1.96	0.40	2.28	0.30	36.45	61.68	74.77
8	W	0.42	0.55	0.41	0.54	95.52	99.59	99.90
	C	0.50	0.40	0.51	0.35	90.80	98.98	99.69

can be feasibly predicted by fitting the model using five oceanic front structures and acoustic field environmental factors. Experimental results indicated that the predicted distances followed the same trend as the training set, with superior prediction performance in August. The proportion of data with a prediction error of less than 3 km for the convergence zone distance exceeded 90%, and for the short-range detection distance, it accounted for ~80% of the total data.

5. Conclusions

In this study, JCOPE2M, a high-resolution ocean reanalysis product, was utilized to determine the depth of the maximum intensity of the KEF based on the horizontal absolute gradient. Subsequently, three months with different KEF intensities were selected, and environmental parameters and underwater acoustic propagation parameters were constructed using the DP algorithm and the Bellhop underwater acoustic propagation model. Through analysis, the effects of the KEF on underwater acoustic propagation were revealed. Moreover, a BP neural network with 2 hidden layers, each containing 12 hidden layer nodes, was constructed to model and forecast the convergence zone distance based on five factors. The primary findings of this study are:

(1) Our analysis revealed that the strength of KEF follows an increasing-then-decreasing pattern as the depth increases. The highest frequency of the most intense KEF occurred in the water layer with a depth of 300–400 m, showcasing a maximum strength ranging from 0.7656 to 0.8395°C/km. Nevertheless, the frequency of the strongest KEF tended to be zero in the water layer with a depth exceeding 800 m.

(2) This study primarily focused on two acoustic propagation parameters: the short-range detection distance and the FCZ distance. The influence of the KEF is more pronounced when the sound source is located on the warm-water side. The correlation between the horizontal temperature and salinity gradient on the warm-water side and the acoustic propagation factors is superior compared to the cold-water side, ranging from 0 to 0.3. When examining the short-range detection distance, significant seasonal effects are observed. In winter, the impact on the short-range detection distance is significant, with a maximum correlation of 0.86, whereas in July and August, the correlation is weaker. The significant factors influencing the FCZ distance are the acoustic channel axis depth and the vertical gradient of the transition layer of sound speed discontinuity. The former demonstrated a correlation with the FCZ distance ranging from 0.52 to 0.82, whereas the latter ranged from −0.42 to −0.7. The horizontal temperature and salinity gradient are the subsequent influencing factors. The correlation of the temperature gradient is higher than that of the salinity gradient, with the difference ranging from 0 to 0.13. Under weak front conditions, the temperature and salinity gradient may exhibit weak or no correlation with underwater acoustic propagation.

(3) There is considerable potential for using neural networks in forecasting the convergence zone distance. Based on the constructed sequences of ocean and acoustic environmental parameters, the BP neural network can achieve good fitting and prediction of the convergence zone distance in ocean front environments. The prediction performance in August surpasses that in February, and the prediction accuracy is the highest when the sound source is located on the cold-water side. The frequency of the prediction distance error less than 3 km exceeds 90%, and the highest frequency with an error less than 1 km is 68.61%.

The correlation between the vertical temperature and salinity gradient and underwater acoustic propagation in this study depends on the modeling approach. To avoid the mutual influence among the analyzed environmental parameters, the KEF was segmented for analysis, which introduced some discrepancies from the actual KEF. However, these deviations did not impact the proposed approach for underwater acoustic propagation prediction based on the environmental parameters outlined in this study. Future research should focus on improving the selection and discrimination of the environmental parameters by utilizing more accurate modeling and feature extraction methods to enhance prediction accuracy.

Acknowledgments

This research was supported by the Dalian Naval Academy Research and Development Fund. The authors would like to express their sincere gratitude to the National Ocean Partnership Program (NOPP) and National Centers for Environmental Information for providing several years of current (https://data.hycom.org) and bathymetry data (https://www.ncei.noaa.gov). We are also grateful to the Japan Agency for Marine-Earth Science and Technology for their support in providing the JCOPE2M data (https://www.jamstec.go.jp), particularly to Mr. RuoChao Zhang for his assistance with processing the JCOPE2M data. Finally, we would like to acknowledge the assistance provided by other scholars and institutions who helped us during the course of this research.

References

1. Amante C., Eakins B.W. (2009), ETOPO1 1 Arc-Minute Global Relief Model: Procedures, data sources and analysis. NOAA technical memorandum NESDIS NGDC-24, *National Geophysical Data Center*, doi: 10.7289/V5C8276M.

2. Chang Y.-L., Miyazawa Y., Guo X. (2015), Effects of the STCC eddies on the Kuroshio based on the 20-year JCOPE2 reanalysis results, *Progress in Oceanography*, **135**: 64–76, doi: 10.1016/j.pocean.2015.04.006.

3. Chang Y.-L.K., Miyazawa Y., Béguer-Pon M., Han Y.-S., Ohashi K., Sheng J. (2018), Physical and biological roles of mesoscale eddies in Japanese eel larvae dispersal in the western North Pacific Ocean, *Scientific Reports*, **8**(1): 503, doi: 10.1038/s41598-018-23392-5.

4. Chassignet E.P. *et al.* (2007), The HYCOM (HYbrid Coordinate Ocean Model) data assimilative system, *Journal of Marine Systems*, **65**(1–4): 60–83, doi: 10.1016/j.jmarsys.2005.09.016.

5. Chen C., Yang K., Duan R., Ma Y. (2017), Acoustic propagation analysis with a sound speed feature model in the front area of Kuroshio Extension, *Applied Ocean Research*, **68**: 1–10, doi: 10.1016/j.apor.2017.08.001.

6. Chen S. (2008), The Kuroshio Extension Front from satellite sea surface temperature measurements, *Journal of Oceanography*, **64**(6): 891–897, doi: 10.1007/s10872-008-0073-6.

7. Cheney R.E., Winfrey D. (1976), Distribution and classification of ocean fronts, *U.S. Naval Oceanographic Office*, Washington D.C.

8. Doan V.-S., Huynh-The T., Kim D.-S. (2020), Underwater acoustic target classification based on dense convolutional neural network, *IEEE Geoscience and Remote Sensing Letters*, **19**: 1–5, doi: 10.1109/LGRS.2020.3029584.

9. Dong S., Sprintall J., Gille S.T. (2006), Location of the Antarctic Polar Front from AMSR-E satellite sea surface temperature measurements, *Journal of Physical Oceanography*, **36**: 2075–2089, doi: 10.1175/JPO2973.1.

10. Dreini G., Jensen F.B. (1990), Sound propagation through an oceanic front, *Journal de Physique Colloques*, **51**(C2): 1025–1028, doi: 10.1051/jphyscol:19902240.

11. Hamilton E.L. (1980), Geoacoustic modeling of the sea floor, *The Journal of the Acoustical Society of America*, **68**(5): 1313–1340, doi: 10.1121/1.385100.

12. Etter P.C. (2013), *Underwater Acoustic Modeling and Simulation*, 4th ed., CRC Press, Taylor & Francis Group.

13. Kida S. *et al.* (2015), Oceanic fronts and jets around Japan: A review, *Journal of Oceanography*, **71**: 469–497, doi: 10.1007/s10872-015-0283-7.

14. Lee-Leon A., Yuen C., Herremans D. (2021), Underwater Acoustic Communication Receiver Using Deep Belief Network, *IEEE Transactions on Communications*, **69**(6): 3698–3708, doi: 10.1109/TCOMM.2021.3063353.

15. Lee B.M., Johnson J.R., Dowling D.R. (2022), Neural network predictions of acoustic transmission loss uncertainty, *The Journal of the Acoustical Society of America*, **152**(4): 152, doi: 10.1121/10.0015877.

16. Liu J., Piao S., Zhang, M., Zhang S., Guo J., Gong L. (2021), Characteristics of three-dimensional acoustic propagation in Western North Pacific Fronts, *Journal of Marine Science and Engineering*, **9**(9): 1035, doi: 10.3390/jmse9091035.

17. Liu J., Zhang Y., Zhang X. (2015), Analysis on the characteristics of the spatial and temporal variation of the Kuroshio Extension Front and the distribution of the sound field [in Chinese], *Journal of Ocean Technology*, **34**(02): 15–20, http://hyjsxb.cnjournals.org/ch/reader/view_abstract.aspx?file_no=20150203&flag=1.

18. Liu Z.-J., Nakamura H., Zhu X.-H., Nishina A., Guo X., Dong M. (2019), Tempo-spatial variations of the Kuroshio current in the Tokara Strait based on long-term ferryboat ADCP data, *Journal of Geophysical Research: Oceans*, **124**(8): 6030–6049, doi: 10.1029/2018JC014771.

19. Mellberg L.E., Johannessen O.M., Connors D.N., Botseas G., Browning D.G. (1991), Acoustic propagation in the western Greenland Sea frontal zone, *The Journal of the Acoustical Society of America*, **89**(5): 2144–2156, doi: 10.1121/1.400908.

20. Miyazawa Y. *et al.* (2017), Assimilation of high-resolution sea surface temperature data into an operational nowcast/forecast system around Japan using a multi-scale three-dimensional variational scheme, *Ocean Dynamics*, **67**(6): 713–728, doi: 10.1007/s10236-017-1056-1.

21. Miyazawa Y. *et al.* (2019), Temperature profiling measurements by sea turtles improve ocean state estimation in the Kuroshio-Oyashio Confluence region, *Ocean Dynamics*, **69**(2): 267–282, doi: 10.1007/s10236-018-1238-5.

22. Ozanich E., Gawarkiewicz G., Lin Y.-T. (2022), Study of acoustic propagation across an oceanic front at the edge of the New England shelf, *The Journal of the Acoustical Society of America*, **152**(6): 3756, doi: 10.1121/10.0016630.

23. Porter M.B. (2011), *The BELLHOP Manual and User's Guide: Preliminary Draft*, Heat, Light, and Sound Research, Inc., USA.

24. Rousseau T.H., Siegmann W.L., Jacobson M.J. (1982), Acoustic propagation through a model of shallow fronts in the deep ocean, *The Journal of the Acoustical Society of America*, **72**(3): 924–936, doi: 10.1121/1.388173.

25. Seo Y., Sugimoto S., Hanawa K. (2014), Long-Term variations of the Kuroshio Extension Path in winter: Meridional movement and path state change, *Journal of Climate*, **27**(15): 5929–5940, doi: 10.1175/JCLI-D-13-00641.1.

26. Shapiro G., Chen F., Thain R. (2014), The effect of ocean fronts on acoustic wave propagation in the Celtic Sea, *Journal of Marine Systems*, **139**: 217–226, doi: 10.1016/j.jmarsys.2014.06.007.

27. Sugimoto S., Kobayashi N., Hanawa K. (2014), Quasi-decadal variation in intensity of the western part of the winter subarctic SST Front in the Western North Pacific: The influence of Kuroshio extension path state, *Journal of Physical Oceanography*, **44**(10): 2753–2762, doi: 10.1175/JPO-D-13-0265.1.

28. Urick R.J. (1975), Principles of Underwater Sound, 3rd ed., McGraw-Hill, New York, London.

29. Wang J., Mao K., Chen X., Zhu K. (2020), Evolution and structure of the Kuroshio extension front in spring 2019, *Journal of Marine Science and Engineering*, **8**(7): 502, doi: 10.3390/jmse8070502.

30. Wang Y., Yang X., Hu J. (2016), Position variability of the Kuroshio Extension sea surface temperature front, *Acta Oceanologica Sinica*, **35**(07): 30–35, doi: 10.1007/s13131-016-0909-7.

31. Yasuda I. (2003), Hydrographic structure and variability in the Kuroshio-Oyashio transition area, *Journal of Oceanography*, **59**(4): 389–402, doi: 10.1023/A:1025580313836.

32. Yu P., Zhang L., Liu M., Zhong Q., Zhang Y., Li X. (2020), A comparison of the strength and position variability of the Kuroshio Extension SST front, *Acta Oceanologica Sinica*, **39**(5): 26–34, doi: 10.1007/s13131-020-1567-3.